

Self-Powered Piezo-Supercapacitors Based on ZnO@Mo-Fe-MnO₂ Nanoarrays

Luo Sun¹, Zhiguo Ye¹, Xinyuan Peng¹, Shaojie Zhuang¹, Duosheng Li¹, and Zhong Jin²

¹Nanchang Hangkong University

²Nanjing University

August 7, 2023

Abstract

The development of self-charging supercapacitor power cells (SCSPCs) has profound implications for smart electronic devices used in different fields. Here, we epitaxially electrodeposited Mo- and Fe-codoped MnO₂ films on piezoelectric ZnO nanoarrays (NAs) grown on the flexible carbon cloth (denoted ZnO@Mo-Fe-MnO₂ NAs). An SCSPC device was assembled with the ZnO@Mo-Fe-MnO₂ NA electrode and poly(vinylidene fluoride-co-trifluoroethylene) (PVDF-Trfe) piezoelectric film doped with BaTiO₃ (BTO) and carbon nanotubes (CNTs) (denoted PVDF-Trfe/CNTs/BTO). The SCSPC device exhibited an energy density of 30 $\mu\text{Wh cm}^{-2}$ with a high-power density of 40 mW cm^{-2} , and delivered an excellent self-charging performance of 363 mV (10 N) driven by both the piezoelectric ZnO NAs and the PVDF-Trfe/CNTs/BTO films. More intriguingly, the device also could also be self-charged by 184 mV due to residual stress alone, and showed excellent energy conversion efficiency and low self-discharge rate. This work illustrates for the first time the self-charging mechanism involving electrolyte ion migration driven by both electrodes and films. A comprehensive analysis strongly confirmed the important contribution of the piezoelectric ZnO NAs in the self-charging process of the SCSPC device. This work provides novel directions and insights for the development of SCSPCs.

Self-Powered Piezo-Supercapacitors Based on ZnO@Mo-Fe-MnO₂ Nanoarrays

Luo Sun,^{1,#} Zhiguo Ye,^{*,1} Xinyuan Peng,¹ Shaojie Zhuang,¹ Duosheng Li,¹ Zhong Jin^{*,2}

¹ School of Materials Science and Engineering, Nanchang Hangkong University, 696#, FengHeNan Road, Nanchang 330063, China

² State Key Laboratory of Coordination Chemistry, MOE Key Laboratory of Mesoscopic Chemistry, MOE Key Laboratory of High Performance Polymer Materials and Technology, Jiangsu Key Laboratory of Advanced Organic Materials, School of Chemistry and Chemical Engineering, Nanjing University, Nanjing, Jiangsu 210023, China.

*Correspondence and requests for materials should be addressed to Z. G. Ye (email: yezhihuo2008@163.com) or to Z. Jin (email: zhongjin@nju.edu.cn).

Acknowledgements

The authors are grateful to the supports by the Key Research and Development Program of Jiangxi Province (20203BBE53069), the National Key R&D Program of China (2017YFA0208200), the National Natural Science Foundation of China (51862026, 22022505 and 21872069), the Fundamental Research Funds for the Central Universities of China (02051438026, 020514380272 and 020514380274), the Scientific and Technological Innovation Special Fund for Carbon Peak and Carbon Neutrality of Jiangsu Province (BK20220008),

the Natural Science Foundation of Jiangxi Province (20192ACBL21048), the Nanjing International Collaboration Research Program (202201007 and 2022SX00000955), and the Suzhou Gusu Leading Talent Program of Science and Technology Innovation and Entrepreneurship in Wujiang District (ZXL2021273).

Abstract

The development of self-charging supercapacitor power cells (SCSPCs) has profound implications for smart electronic devices used in different fields. Here, we epitaxially electrodeposited Mo- and Fe-codoped MnO_2 films on piezoelectric ZnO nanoarrays (NAs) grown on the flexible carbon cloth (denoted ZnO@Mo-Fe- MnO_2 NAs). An SCSPC device was assembled with the ZnO@Mo-Fe- MnO_2 NA electrode and poly(vinylidene fluoride-co-trifluoroethylene) (PVDF-Trfe) piezoelectric film doped with BaTiO_3 (BTO) and carbon nanotubes (CNTs) (denoted PVDF-Trfe/CNTs/BTO). The SCSPC device exhibited an energy density of $30 \mu\text{Wh cm}^{-2}$ with a high-power density of 40 mW cm^{-2} , and delivered an excellent self-charging performance of 363 mV (10 N) driven by both the piezoelectric ZnO NAs and the PVDF-Trfe/CNTs/BTO films. More intriguingly, the device also could also be self-charged by 184 mV due to residual stress alone, and showed excellent energy conversion efficiency and low self-discharge rate. This work illustrates for the first time the self-charging mechanism involving electrolyte ion migration driven by both electrodes and films. A comprehensive analysis strongly confirmed the important contribution of the piezoelectric ZnO NAs in the self-charging process of the SCSPC device. This work provides novel directions and insights for the development of SCSPCs.

KEYWORDS: Self-charging; Supercapacitors; Piezoelectric; ZnO nanoarray; MnO_2

Introduction

With the advent of the Internet of Things and the artificial intelligence era, the rapid development of microelectromechanical systems has brought great convenience to peoples' lives^[1]. These energy devices have received much attention because they are well suited for implantable medical devices (*e.g.*, pacemakers), wearable electronic devices, high-precision sensors, and other equipment^[2, 3]. However, frequent charging and replacement of the conventional batteries and their inability to provide a continuous power supply has drastically hindered commercial applications^[4, 5]. To address this issue, it is intriguing to develop self-charging supercapacitor power cells that can directly convert mechanical energy into electrochemical energy by integrating the energy harvesting devices and storage devices internally^[6, 7]. The SCSPCs hold great potential for both micro (*e.g.*, electronic skin and biosensors) and macro (*e.g.*, electric transport vehicles and health monitoring systems) device applications^[8, 9]. Supercapacitors (SCs) are considered to be potential next-generation candidates for energy storage devices because of their fast charge/discharge rates, long lifespans, high power densities, low costs, and safer operability compared to other batteries^[10]. In particular, in previous studies of SCSPCs, supercapacitors and nanogenerators were successfully integrated to charge the supercapacitors directly from external forces without rectifiers^[11]. However, the integrated SCSPCs usually suffer from low self-charging voltages and low energy conversion efficiencies. Moreover, the problem of self-discharge, which usually exists in ordinary SCs, is still of significant concern with the SCSPCs^[12]. These problems limit the application of SCSPCs, and must be addressed carefully.

In addition, the choice of SCSPC electrode materials has a significant impact on the performances of both energy storage and self-charging. Previous study has shown that the choice of SCSPC electrode materials is basically the same as that of ordinary SCs, and the goal is to obtain excellent energy storage performance with minimal to zero impact on the self-charging process^[13]. To address this problem, Iqra Rabani et al^[14]. prepared a BNNT-CNF/ZnO electrode that was a composite of three materials: cellulose nanofibers (CNFs), boron nitride nanotubes (BNNTs), and ZnO nanoparticles. It had a specific capacitance of 300 F g^{-1} (1 A g^{-1}) and a piezoelectric coefficient of -12.6 pC N^{-1} . Bhavya Padha et al^[15]. assembled an SCSPC with perovskite NiSnO_3 as the positive electrode, FeSnO_3 as the negative electrode, and a PVA-KOH electrolyte. The device could be self-charged to 266 mV at an applied force of 20 N, and showed an energy density of 45 Wh kg^{-1} at a power density of 1.25 kW kg^{-1} . Overall, it is crucial to design new nanocomposite electrode materials that can simultaneously provide a good piezoelectric response and excellent energy storage performance.

MnO₂ is widely used as an electrode of supercapacitors because of its abundance of resources, lower cost, environmental soundness, and high theoretical specific capacitance of 1370 F g⁻¹[16, 17]. However, the inferior conductivity and inefficiency of MnO₂ hamper its use in supercapacitors[18]. Previous studies have found that the use of metal ion doping (*e.g.*, Mo, Fe, Au, Ag) to adjust the crystal electron cloud orbitals, narrow the forbidden band width, constitute nonintrinsic semiconductors or nanocarbon material dopants (*e.g.*, carbon nanotubes, graphene) to form conducting channels and heterogeneous structures could effectively tackle the issue of low conductivity for MnO₂[19, 20]. The inefficiency of MnO₂ utilization could also be effectively solved by increasing its specific surface area[21]. ZnO is a hemimorphite piezoelectric material with high stability, a high mechanical quality factor and a considerable specific surface area, which facilitates the transformation of mechanical energy towards electrochemical energy to a certain extent[22, 23]. ZnO has been used as a filler compounded with PVDF to form a piezoelectric film that utilizes the piezoelectric properties of ZnO, but the excellent nanostructure of ZnO was not effectively utilized[24, 25]. If ZnO and ion-doped MnO₂ can be effectively combined as composite electrode materials for SCSPCs via a simple method, the surface area of ion-doped MnO₂ will be increased by using ZnO nanostructures. In this way, the special morphologies of ZnO nanoarrays and their piezoelectric properties will be fully utilized, and the problems of inferior conductivity and inefficiency for MnO₂ will be effectively solved.

In this study, we report the development of an SCSPC with a high charging voltage and excellent energy conversion efficiency. ZnO nanoarrays were used as the current collectors to expand the effective surface area of the MnO₂ layer doped with Mo and Fe ions[26]. Additionally, the utilization of ZnO and piezoelectric films to drive the migration of electrolyte ions gave the SCSPC a larger self-charging voltage and higher energy conversion efficiency. Interestingly, the presence of ZnO enabled the SCSPC to self-charging by residual stress[27], and the self-discharge rate was significantly reduced, which provides useful support for practical applications of SCSPCs. Moreover, self-charging via electrolyte ion migration driven by both the electrode and the film is demonstrated for the first time in this work, and it provides strong evidence for the great contributions of ZnO.

Results and discussion

Figure 1a-c shows a summary of the process used to prepare ZnO@Mo-Fe-MnO₂ NAs on the flexible carbon cloth (CC), PVDF-Trfe/CNTs/BTO piezoelectric film and SCSPC devices. Here, the ZnO@Mo-Fe-MnO₂ NA electrode was prepared with a two-step electrodeposition method (Figure 1a). First, the ZnO nanoarrays with a mass of approximately 1.1 mg were grown on the CC via the cathodic electrodeposition method. After that, a Mo and Fe ion-doped MnO₂ film with a load of 1.1 mg was epitaxially codeposited on the ZnO nanoarrays via anodic electrodeposition, and ZnO@Mo-Fe-MnO₂ NAs were formed on the flexible CC. PVDF-Trfe/CNTs/BTO piezoelectric films with arranged micropores were prepared by the casting method (see Figure 1b) [28, 29]. The piezoelectric film functioned as both a separator and an energy harvester[30]. Figure 1c shows the entire structure of the SCSPC device assembled from ZnO@Mo-Fe-MnO₂ NA electrodes and PVDF-Trfe/CNTs/BTO piezoelectric thin films. The electrode and separator were filled with the H₃PO₄ electrolyte and bonded.

Characterization of electrode materials

Figure 1d shows the X-ray diffraction (XRD) patterns for CC@Mo-Fe-MnO₂ (electrodeposited Mo- and Fe-doped MnO₂ films on CC), ZnO@Mo-Fe-MnO₂ NAs, ZnO@Mo-MnO₂ NAs (epitaxially electrodeposited Mo-doped MnO₂ films on ZnO NAs), ZnO@MnO₂ NAs (epitaxially electrodeposited MnO₂ films on ZnO NAs), and CC/ZnO NAs (electrodeposited ZnO NAs on CC). As shown in the figure, the diffraction peaks seen at 25.8° and 43.4° for all of the as-prepared samples were those of the CC (JCPDS No. 75-1621)[31]. The weak diffraction peaks located at 31.8° and 34.4° corresponded to the (100) and (002) crystal planes of ZnO, respectively, owing to overlap with the MnO₂ film on the surface (JCPDS No. 99-0111). The remaining peaks at 35.2°, 38.6°, 53.0°, 60.5°, and 65.4° corresponded to the (310), (111), (121), (321) and (002) crystal planes of MnO₂, respectively (JCPDS No. 72-1983). Obviously, doping of the Mo and Fe ions into the bulk MnO₂ did not change the structure owing to the small doping levels.

Figure 1e shows field emission scanning electron microscopy (SEM) images of the flexible CC and CC/ZnO NAs. The ZnO NAs grew uniformly on the CC surface and formed an ordered three-dimensional (3D) NA structure. Figure 1f shows the surface morphologies of the ZnO@Mo-Fe-MnO₂ NAs. The Mo and Fe ion-doped MnO₂ tightly wrapped the ZnO NAs and formed a hexagonal prism-shaped ZnO@Mo-Fe-MnO₂ NAs. The ZnO nanoarrays provided a basis for the formation of ZnO@Mo-Fe-MnO₂ NA. Figure S1 demonstrates the homogenous distribution of the ZnO nanoarrays and ZnO@Mo-Fe-MnO₂ NAs throughout the CC as well as the hexagonal prism shapes of the ZnO@Mo-Fe-MnO₂ NAs. Mo ion doping formed the 3D nanoarray with the tubular structure, as shown in Figure S2-4. Fe ion doping transformed the original tubular structure to a hexagonal prismatic structure.

X-ray photoelectron spectroscopy (XPS) analyses were used to identify the elemental compositions and valence states of the ZnO@Mo-Fe-MnO₂ NAs. Figure S5 indicates the presence of C, O, Mn, Mo, Fe and Zn in the ZnO@Mo-Fe-MnO₂ NAs. Figure 2a shows the Mn 2p XPS data for the ZnO@Mo-Fe-MnO₂ NA electrode. The high-resolution Mn 2p spectrum contained two peaks at 653.9 and 642.7 eV, which corresponded to the binding energies of the Mn 2p_{1/2} and Mn 2p_{3/2} states, respectively^[32, 33]. The spin orbit separation was 11.2 eV, and the signals corresponded to the Mn⁴⁺ species in MnO₂, which was consistent with the phases indicated by XRD. Figure 2b shows the high-resolution Mo 3d spectrum. As displayed in the figure, the peaks located at 235.6 and 232.4 eV corresponded to the Mo 3d_{3/2} and Mo 3d_{5/2} states with a splitting of 3.15 eV, respectively, which was assigned to Mo⁶⁺^[34]. In Figure 2c, the high-resolution Fe 2p spectrum contained two peaks exhibiting spin-orbit splitting and two accompanying satellite (Sat) peaks. Among these, the peaks located at 725.6 and 712.5 eV corresponded to the Fe 2p_{1/2} and Fe 2p_{3/2} states, respectively, and exhibited a spin-orbit splitting energy of 13.1 eV. The peaks located at 730.4 and 719.0 eV were identified as the accompanying satellite peaks^[35]. This proved that Fe was present in the form of Fe³⁺ ions in the electrode. Figure 2d shows that the peaks located at 1044.8 and 1021.8 eV corresponded to the Zn 2p_{1/2} and Zn 2p_{3/2} states, respectively. The spin-orbit splitting energy of 23 eV corresponded to the Zn²⁺ in ZnO^[36], which was consistent with the XRD results. The high-resolution O 1s spectrum shown in Figure 2e was deconvoluted into four peaks (O1, O2, O3, O4). They were derived from Mn-O-Mn bonds (530.2 eV, O1), Zn-O bonds (531.1 eV, O2), Mo-O bonds (529.7 eV, O3), and Fe-O bonds (532.3 eV, O4). Interestingly, the peak areas of O1 and O2 were larger than those of O3 and O4, which perfectly matched the component contents in the ZnO@Mo-Fe-MnO₂ NA electrode.

Figure 2f-g shows transmission electron microscopy (TEM) and scanning TEM (STEM) images of the ZnO@Mo-Fe-MnO₂ NA electrode. The hexagonal prismatic structure of the ZnO@Mo-Fe-MnO₂NAs can be seen in the figure. The hexagonal ZnO prisms were surrounded by the Mo- and Fe-ion-doped MnO₂. Figure 2h-i shows a high-resolution TEM (HRTEM) image of the ZnO@Mo-Fe-MnO₂NA electrode. The analysis showed that the interplanar distances of 0.23 and 0.25 nm corresponded to the (111) and (310) crystal planes of MnO₂, respectively. The interplanar distances of 0.28 and 0.26 nm corresponded to the (100) and (002) crystal planes of ZnO, respectively. This once again confirmed the successful synthesis of the ZnO@Mo-Fe-MnO₂ NA heterostructure, and the conclusions were entirely consistent with the XRD analyses. Selected area electron diffraction (SAED) images are shown in Figure S6. Most of the regions in the high-resolution TEM images were amorphous, which indicated the excellent electrochemical performance of the electrode^[37]. Figure 2j-n shows the energy dispersive X-ray (EDX) element maps for the selected area of the ZnO@Mo-Fe-MnO₂ NA electrode. This figure illustrates the evenly distributed of Mn, Mo, Fe, Zn and O in the ZnO@Mo-Fe-MnO₂ NA electrode.

Electrochemical performances of electrode materials

Cyclic voltammetry (CV) measurements were used to evaluate the electrochemical properties of all as-prepared electrodes. Figure 3a shows the CV curves generated for all of the electrodes with scan rates of 100 mV s⁻¹. It is clear that the ZnO@Mo-Fe-MnO₂ NA electrode had the largest CV-active area and exhibited the highest specific capacitance at an ultrahigh scan rate. In the galvanostatic charge-discharge (GCD) curves for the electrodes (Figure 3b), the discharge time for the ZnO@Mo-Fe-MnO₂ NA (332.5 s) electrode was far longer than those of the ZnO@MnO₂ NA (156.3 s), ZnO@Mo-Mn₂ NA (267.6 s) and CC@Mo-Fe-

MnO₂ (199.3 s) electrodes, which indicated the largest specific capacitance. Electrochemical impedance measurements (EIS) analyses were performed for evaluated the electrochemical kinetics from all as-prepared electrodes. In the high-frequency region, the Nyquist plot intercepted with the real axis was the equivalent series resistances (R_s) for the electrodes, which arose from the internal resistances of the electrolyte and the electrodes itself^[38]. The half-circle in the high- to mid-frequency region represented the charge transfer resistance (R_{ct}). A smaller semicircle diameter indicates a lower resistance to charge transfer from the electrolyte to the electrode surface^[39]. The slope of the straight line in the low frequency region indicates the Warburg impedance (R_w) of the electrode, and the greater the slope, the less resistance of electrolyte ions diffusion into the electrode material^[40]. As shown in Figure 3c, the ZnO@Mo-Fe-MnO₂ NAs exhibited the smallest semicircle diameter in the mid-high frequency region. This indicated that the ZnO@Mo-Fe-MnO₂ NAs had the smallest resistance to ion diffusion from the electrolyte to the electrode material^[41]. Moreover, the ZnO@Mo-Fe-MnO₂ NA electrode had the smallest R_s and R_w . This indicated that doping with the Mo and Fe ions improved the electrical conductivity of MnO₂ and reduced the internal resistance of the electrode and the resistance to diffusion of the electrolyte ions into MnO₂^[42]. In summary, the ZnO@Mo-Fe-MnO₂ NA electrode showed the largest specific capacitance and much better electrochemical performance than other electrodes. The reasons for this can be attributed to the following: (1) the ZnO nanoarrays provided a larger surface area for the growth of MnO₂ and formed strongly bound ZnO@Mo-Fe-MnO₂ NAs. This special micromorphology withstood the volume changes occurring during long-term charging and discharging and improved the effective area of the active material (MnO₂) and shortened the ion diffusion paths between the electrode and the electrolyte^[43, 44]. (2) Doping of the Mo and Fe ions improved the electrical conductivity of MnO₂, accelerated charge transfer in the electrode and thus increased the specific capacitance of the electrode^[45, 46]. (3) The combined crystalline and amorphous nanostructures in the ZnO@Mo-Fe-MnO₂ NA electrode exposed many defects, provided more active sites for the faradic processes and thus increased the specific capacitance of the electrode^[44, 47].

Figure 3d shows that CV curves of the ZnO@Mo-Fe-MnO₂ NA electrode obtained at different scan rates of 2–100 mV s⁻¹. All of the voltammograms were rectangular in shape and highly symmetric. This showed that the electrode was mainly contributed by the bilayer capacitance and had a reversible Faraday effect and high Coulombic efficiency^[48]. Figure 3e shows that GCD curves for the ZnO@Mo-Fe-MnO₂ NA electrode with different current densities from 1–100 A g⁻¹. All of the curves were symmetrical and triangular in shape and exhibited no significant voltage drops, which meant excellent specific capacitance and high transfer rates. The CV and GCD curves for the other electrodes are shown in Figure S7-9. Figure 3f compares the capacitances of all electrodes at different current densities from 1–100 A g⁻¹. The specific values are given in Table S1. The ZnO@Mo-Fe-MnO₂ NA electrode showed a high specific capacitance of 415.6 F g⁻¹ at a current density of 1 A g⁻¹ and still exhibited a specific capacitance of 250 F g⁻¹ with an extremely high current density of 100 A g⁻¹. The ZnO@Mo-Fe-MnO₂ NA electrode had the largest mass (415.6 F g⁻¹), area (457.2 mF cm⁻²) and volume (14.3 F cm⁻³) specific capacitance among the prepared electrodes (Figure 3g). In addition, it had the highest capacitance retention rate (60.2%), which is detailed in Figure S10. The electrodes exhibited both double layer capacitance and Faraday capacitance during energy storage. Among them, the Faraday capacitance is controlled by ion diffusion^[49]. Therefore, its capacitive contribution was calculated (Figure 3h and Figure S11). Since doping with Mo and Fe enhanced the conductivity of the electrode, it showed a higher capacitance contribution. The ZnO@Mo-Fe-MnO₂ NA electrode contributed up to 87.4% at a scan rate of 100 mV s⁻¹ and still had a contribution of 61.2% at a scan rate of 5 mV s⁻¹. This proved that the capacitance of the electrodes was mainly dominated by the bilayer capacitance, which was consistent with the above analysis. Figure 3i displays the stability of the ZnO@Mo-Fe-MnO₂ NA electrode after 10,000 cycles at a current density of 10 A g⁻¹. The results showed that the electrodes still retained 83.6% of the original capacitance and exhibited approximately 100% Coulombic efficiency after 10,000 cycles. Interestingly, the electrode still retained the original NA morphology after cycling (Figure S12). The remarkably long cycling stability was attributed to strong binding of the ZnO@Mo-Fe-MnO₂ NAs and the special microscopic morphologies of the electrodes. This morphology was instrumental in reducing the internal stresses generated during cycling and the resulting volume changes.

Energy storage performances of SCSPC

To probe the electrochemical performance further, a symmetric ZnO@Mo-Fe-MnO₂ NA SCSPC was generated with ZnO@Mo-Fe-MnO₂ NA electrodes, the H₃PO₄/PVA gel electrolyte and a PVDF-Trfe/CNTs/BTO piezoelectric separator. For comparison, CC@Mo-Fe-MnO₂ SCSPC devices without the ZnO NAs were also assembled. Since the ionic conductivity of PVDF-Trfe ($3.10 \times 10^{-4} \text{ S cm}^{-1}$)^[50] was much lower than that of PVA ($1.1 \times 10^{-2} \text{ S cm}^{-1}$)^[51], the PVDF-Trfe/CNT/BTO piezoelectric separator required pore formation before assembly. When assembled, the micropores of the PVDF-Trfe/CNTs/BTO piezoelectric separator were completely filled with the H₃PO₄/PVA gel electrolyte, which significantly improved the ionic conductivity of the piezoelectric film and the electrochemical performance of the SCSPC. Figure 4a-b displays the CV and GCD curves for the ZnO@Mo-Fe-MnO₂ NA SCSPC with different scan rates and current densities. It is noteworthy that none of the CV curves had obvious redox peaks, the GCD curves were nearly symmetric and triangular, and all of the curve shapes were observed with different scan rates and current densities. These results displayed the high reversibility of the assembled SCSPC and were still dominated by the contribution of the typical bilayer capacitance. Obviously, the SCSPC had a larger CV curve area and a longer charge/discharge time than the CC@Mo-Fe-MnO₂ SCSPC (Figure S13) at the same scan rate and current density, which again confirmed the great role played by the ZnO nanoarrays in the electrodes. Moreover, the ZnO@Mo-Fe-MnO₂ NA SCSPC exhibited a remarkably large specific capacitance of $810 \mu\text{F cm}^{-2}$ at a current density of $30 \mu\text{A cm}^{-2}$ and still showed a specific capacitance of $337.5 \mu\text{F cm}^{-2}$ with a high current density of $100 \mu\text{A cm}^{-2}$ (Figure S14). It is worth noting that three ZnO@Mo-Fe-MnO₂ NA SCSPCs combined in series lit up a red LED (Figure 4c). This indicated that the ZnO@Mo-Fe-MnO₂ NA SCSPC has excellent electrochemical properties. On the other hand, the long-term cycling stabilization of the ZnO@Mo-Fe-MnO₂ NA SCSPC was evaluated with a current density of $30 \mu\text{A cm}^{-2}$. The results showed 94.3% capacitance retention after 2000 cycles (Figure S15). This proved that the ZnO@Mo-Fe-MnO₂ NA SCSPC had excellent recyclability. In addition, the ZnO@Mo-Fe-MnO₂ NA SCSPC exhibited a better energy storage capability than the CC@Mo-Fe-MnO₂SCSPC (Figure 4d). The Ragone plot in Figure 4d shows that the ZnO@Mo-Fe-MnO₂ NA SCSPC had a high energy density of $72 \mu\text{Wh cm}^{-2}$ with a corresponding power density of 12 mW cm^{-2} at a current density of $30 \mu\text{A cm}^{-2}$. At a high current density of $100 \mu\text{A cm}^{-2}$, it showed an energy density of $30 \mu\text{Wh cm}^{-2}$ and a corresponding power density of 40 mW cm^{-2} . This was far more useful than the previously reported SCSPC devices, including a graphene SCSPC ($3 \mu\text{Wh cm}^{-2}$ at 1.77 mW cm^{-2})^[52], a graphene PI-SCSPC ($6.27 \mu\text{Wh cm}^{-2}$ at $0.0178 \text{ mW cm}^{-2}$)^[53], a MoSe₂ SCSPC ($10 \mu\text{Wh cm}^{-2}$ at 0.269 mW cm^{-2})^[54], a Co-NPC/LIG/Cu SCSPC ($27.8 \mu\text{Wh cm}^{-2}$ at 0.089 mW cm^{-2})^[55] and a MoS₂-Nafion-MoS₂ SCSPC ($0.019 \mu\text{Wh cm}^{-2}$ at 0.04 mW cm^{-2})^[56].

Characterization and energy-harvesting performances of Piezoelectric films

Figure 5a shows the XRD patterns of the PVDF-Trfe, PVDF-Trfe doped with CNTs (PVDF-Trfe/CNTs) and PVDF-Trfe/CNT/BTO piezoelectric films. The diffraction peaks at 18.6° and 20.3° corresponded to the (202) crystal plane of the α -phase and the (110) crystal plane of the β -phase, respectively^[57, 58]. The β -phase exhibited piezoelectric and ferroelectric properties with the highest potential energy. The α -phase has neither piezoelectric nor ferroelectric properties and has the lowest potential energy. All of the remaining peaks were the diffraction peaks of BaTiO₃ (JCPDS No. 79-2263). Nano-BaTiO₃ was successfully doped into PVDF-Trfe. The peaks corresponding to the CNTs were not found because of the extremely low CNT content. However, the optical image (Figure S16) shows that doping of the CNTs changed the PVDF-Trfe film colour from slightly yellow to black (the same colour as the CNTs). This demonstrated successful doping of the CNTs into PVDF-Trfe. Figure 5b shows an SEM image of the PVDF-Trfe/CNT/BTO piezoelectric film, and this analysis combined with Figure S17-19 showed that the nano-BaTiO₃ and CNTs were uniformly dispersed in PVDF-Trfe. Figure 5c-d displays the open-circuit voltages and short-circuit currents at a pressure of 50 N for all piezoelectric films. The specific values are given in Table S2. The PVDF-Trfe/CNT/BTO piezoelectric films showed the largest open-circuit voltage of 71.6 V and the largest short-circuit current of $0.65 \mu\text{A}$. The analysis showed that the improved performance of the PVDF-Trfe/CNT piezoelectric films was attributable to doping with the carbon nanotubes, which increased the content of the β -phase in the PVDF-Trfe and improved the energy harvesting efficiency and conduction paths of the ions and resulted

in improved piezoelectric properties^[59, 60]. The piezoelectric properties of BaTiO₃($d_{33}=190 \text{ pC N}^{-1}$)^[61] are much better than those of PVDF-Trfe ($d_{33}=38 \text{ pm V}^{-1}$)^[62]. Therefore, the improved performance of PVDF-Trfe/CNTs/BTO piezoelectric films was mainly attributed to doping of the nano-BaTiO₃. The SCSPC devices were therefore assembled with the PVDF-Trfe/CNTs/BTO piezoelectric films.

Self-powered performances of SCSPCs

To investigate the self-charging performance of the ZnO@Mo-Fe-MnO₂ NA SCSPC device, the pressure of 10 N and 3 Hz was used to test the self-charging performance (Figure 6a). The device's voltage increased from 58 mV to 409 mV (self-charging of 351 mV) after continuous pressure for 1800 s. It is noteworthy that the voltage of the device was still increasing after withdrawal of the pressure (yellow area in Figure 6a), and it increased from 409 mV to 421 mV (12 mV self-charged) in 1800–2200 s (400 s). This was attributed to self-charging due to the release of residual stress^[63]. The self-discharge potential of the device was only 9 mV over 2200–3000 s (800 s) (blue area in Figure 6a) in the absence of a continuously applied pressure. Magnified images of the 1800–3000 s self-charging period are shown in Figure S20. To investigate the self-charging mechanism of the ZnO@Mo-Fe-MnO₂ NA SCSPC device more deeply, the self-charging capabilities of CC@Mo-Fe-MnO₂ SCSPC and the CC@Mo-Fe-MnO₂ SC (assembled with a CC@Mo-Fe-MnO₂ electrode and a commercial separator) devices were tested with the same pressure and frequency. As shown in Figure 6b, the CC@Mo-Fe-MnO₂ SCSPC device self-charged by 121 mV in 330 s and immediately self-discharged by 112 mV in 330–440 s (a self-discharge of 9 mV). As shown in Figure S21, the CC@Mo-Fe-MnO₂ SC device did not exhibit self-charging under a continuous pressure lasting for approximately 550 s. It is significant that the ZnO@Mo-Fe-MnO₂ NA SCSPC device had the largest self-charging voltage (363 mV), and there was a self-charging phase generated by the residual stress in the ZnO@Mo-Fe-MnO₂ NA SCSPC but not in the CC@Mo-Fe-MnO₂ SCSPC. In addition, the self-discharge rate of the ZnO@Mo-Fe-MnO₂ NA SCSPC was much lower. The analysis showed that the ZnO@Mo-Fe-MnO₂ NA SCSPC device had the largest self-charging voltage, which was attributable to the synergistic effect of the piezoelectric material ZnO and the PVDF-Trfe/CNTs/BTO piezoelectric film, which together generated more charge distribution on the electrode surface and eventually increased the voltage of the device again. In addition, the residual stress-induced self-charging phenomenon and the lower self-discharge rate were attributed to the presence of ZnO and the special morphology of the ZnO@Mo-Fe-MnO₂ NA heterostructure. Even under residual stress, a potential difference was generated on the ZnO surface, which drove the mobility of electrolyte ions to the MnO₂ surface and generated self-charging. Thus, the self-charging caused by the residual stress partially offset the self-discharge process of the device, so the result was a device with a low self-discharge rate. Collectively, ZnO improved the efficiency of converting mechanical energy into chemical energy.

To investigate further the self-charging performance of the ZnO@Mo-Fe-MnO₂ NA SCSPC resulting from the residual stress, the pressure was withdrawn after a period of continuous force to ensure that the device only self-charged under the residual stress (Figure 6c). The device voltage increased from 100 mV to 284 mV (self-charging of 184 mV) when subjected to a residual stress for 2500 s. This again indicated that the ZnO@Mo-Fe-MnO₂ NA SCSPC had a very high energy conversion efficiency. To examine the self-discharge rate of the ZnO@Mo-Fe-MnO₂ NA SCSPC further, a leakage current test was performed for 3000 s (Figure S22). At the beginning stage, the current of the device dropped rapidly from 0.1 mA to 1.2 μA within 200 s. This was followed by a slow decrease to 0.3 μA over 1200 s (200–1400 s) and the current remained stable. This again demonstrated that the ZnO@Mo-Fe-MnO₂ NA SCSPC had an extremely low self-discharge rate. In summary, the ZnO@Mo-Fe-MnO₂ NA SCSPC device showed efficient self-charging, a high energy conversion efficiency and a very low self-discharge rate, as seen in Table S3.

Forces of 1 N and 10 N and 0.1–3 Hz frequencies were used in self-charging tests of the ZnO@Mo-Fe-MnO₂ NA SCSPC devices. Figure 6d displays the self-charging curves of the device subjected to a 1 N force and different frequencies ranging from 0.1–3 Hz for 180 s. At 0.1, 0.5, 1 and 3 Hz, the device voltage increased from 40 mV to 55, 61, 67 and 69 mV, respectively, which constituted increases of 15, 21, 27 and 29 mV, respectively. In the same environment, the 10 N force raised the device voltage from 54 mV to 81, 94, 107 and 112 mV, which were increases of 27, 40, 53 and 58 mV, respectively (Figure 6e). The self-charging voltage of

the device increased with increasing applied stress and frequency, indicating excellent self-charging at high and low potentials due to the residual stress (see Video S1 and Video S2). Interestingly, the device exhibited excellent self-charging even with a small force of 1 N at 0.1 Hz, which indicated excellent sensitivity. Even with small force changes, the ZnO@Mo-Fe-MnO₂ NA SCSPC still gave immediate feedback (see Figure S23). Figure 6f shows the stepwise self-charging curve of the ZnO@Mo-Fe-MnO₂ NA SCSPC. Under a continuous pressure, the voltage of the device increased rapidly, and when the pressure was removed, the voltage remained essentially constant. This demonstrated that the ZnO@Mo-Fe-MnO₂ NA SCSPC devices converted mechanical energy into chemical energy with excellent reproducibility^[64].

Working mechanism of ZnO@Mo-Fe-MnO₂ NA SCSPC

To understand the role of the ZnO NAs in the self-charging process of the ZnO@Mo-Fe-MnO₂ NA SCSPC, the self-charging mechanism was analysed. As shown in Figure 7a, the device was in electrochemical equilibrium without any external force applied. When an external force was applied to the device, the ZnO and PVDF-Trfe/CNTs/BTO films were polarized due to the piezoelectric effect. Polarization of the ions produced a potential difference on the surface of the ZnO@Mo-Fe-MnO₂ NA electrode owing to the presence of the ZnO NAs and the PVDF-Trfe/CNTs/BTO film. It is assumed that positive and negative piezoelectric potentials were generated at the upper and lower surfaces of the NA electrodes and PVDF-Trfe/CNTs/BTO films, respectively^[6]. In this case, the electrochemical equilibrium of the device was disrupted, and the piezoelectric potential generated by the electrodes and the film caused the electrolyte ions to migrate to the positive and negative electrodes, respectively. As shown in Figure 7b, the positive potential generated above the NA electrode and PVDF-Trfe/CNTs/BTO film drove the migration of cations to the upper electrode, while the negative potential drove the reverse process. The electrolyte ions were simultaneously driven by the PVDF-Trfe/CNTs/BTO film and the NA electrode, so more ions migrated to the electrode surface, which in turn generated a higher self-charging voltage. Although the external stress was removed, the ion migration processes continued due to the residual stress of the device, which meant that the self-charging process continued, as shown in Figure 7c. Figure 7d shows that a new electrochemical equilibrium was finally reached as the residual stress was released. Finally, the potential difference generated by the PVDF-Trfe/CNTs/BTO films and NA electrodes was a consequence of relaxation of the residual stresses. The ions in the electrolyte reversed their migrations and returned to their original states (Figure 7e). It is evident that ZnO increased the driving force for ion migration during self-charging of the device so that the ZnO@Mo-Fe-MnO₂ NA SCSPC developed a higher self-charging voltage. Moreover, the ZnO@Mo-Fe-MnO₂ NA SCSPC had higher sensitivity and a better energy conversion efficiency because it achieved the same electrolyte ion driving force as the CC@Mo-Fe-MnO₂ SCSPC with a smaller external force (Figure S24).

Conclusions

In summary, we successfully electrodeposited Mo- and Fe-codoped MnO₂ films on ZnO NAs to improve their specific capacitance. The SCSPC device assembled with the ZnO@Mo-Fe-MnO₂ NA electrode and the PVDF-Trfe/CNTs/BTO piezoelectric film has demonstrated an energy density of 30 $\mu\text{Wh cm}^{-2}$ at a high power density of 40 mW cm^{-2} . The device realized self-charging voltage of 363 mV under the action of a 10 N external force. Intriguingly, a self-charging voltage of 184 mV was also achieved by the residual stress as the ZnO and piezoelectric films drove the migration of electrolyte ions. Importantly, this work demonstrates for the first time the self-charging mechanism involving electrolyte ion migration driven by both electrodes and films, which provided strong evidence for the crucial contribution of ZnO to the self-charging process. Additionally, three SCSPCs connected in series successfully lit up a red LED, confirming the great potential for smart electronics applications. The development of high-performance SCSPC devices provides important insights for their future use in industry and life activities.

Experimental section

Chemicals and Materials

HCP 330 N CC was sourced from Guangdong Canrd New Energy Technology Co., Ltd (Guangdong, China). Hexamethylene tetramine (C₆H₁₂N₄) obtained from DAMAO Co., Ltd (Tianjin, China). Manganese acetate

tetrahydrate ($\text{MnC}_4\text{H}_6\text{O}_4 \cdot 4\text{H}_2\text{O}$) was purchased from MACKLIN Co., Ltd (Shanghai, China). Zinc nitrate hexahydrate ($\text{Zn}(\text{NO}_3)_2 \cdot 6\text{H}_2\text{O}$), phosphoric acid (H_3PO_4), sodium sulfate anhydrous (Na_2SO_4), ethanol ($\text{CH}_3\text{CH}_2\text{OH}$) and ammonium iron(II) sulfate hexahydrate ($(\text{NH}_4)_2\text{Fe}(\text{SO}_4)_2 \cdot 6\text{H}_2\text{O}$) obtained from Xilong Scientific Co., Ltd (Guangdong, China). Sodium molybdate ($\text{Na}_2\text{MoO}_4 \cdot 2\text{H}_2\text{O}$) was purchased from Tianjing No. 4 Chemical Reagent Factory (Tianjin, China). The multiwalled CNTs and dispersants (TNWDIS) obtained from Chengdu Organic Chemical Co., Ltd., Chinese Academy of Sciences (Chengdu, China). PVDF-Trfe and poly(vinyl alcohol) (PVA) obtained from Shanghai Aladdin Biochemical Technology Co., Ltd (Shanghai, China). *N,N*-dimethylformamide (DMF) obtained from Tianjin Kemiou Chemical Reagent Co., Ltd (Tianjin, China). Nanometre barium titanate obtained from Sinopharm Chemical Reagent Co., Ltd (Beijing, China). All reagents and materials were of analytical grade and were used without further purification.

Preparation of ZnO nanoarrays

The flexible carbon cloth was ultrasonically cleaned in ethanol, a 0.5 mol L^{-1} H_2SO_4 solution and distilled water for 30 min. It was then put into a drying oven at a temperature of $60 \text{ }^\circ\text{C}$ and dried for 12 h. The nanoarray was fabricated via facile electrodeposition with a three-electrode system. The carbon cloth or ZnO nanoarrays served as the working electrode, a carbon rod served as the counter electrode and a saturated calomel electrode (SCE) served as the reference electrode.

The ZnO nanoarrays were synthesized on a carbon cloth with a mixed solution of $0.01 \text{ M Zn}(\text{NO}_3)_2$ and $0.01 \text{ M C}_6\text{H}_{12}\text{N}_4$ and a simple cathodic electrodeposition method. The electrodeposition process was performed for 60 min used a current density of 0.8 mA cm^{-2} . The electrodeposition process was carried out at $70 \text{ }^\circ\text{C}$ and 125 r min^{-1} stirring speed.

Preparation of ZnO@Mo-Fe-MnO₂ NA

$\text{MnC}_4\text{H}_6\text{O}_4 \cdot 4\text{H}_2\text{O}$ (0.021 mol L^{-1}), $(\text{NH}_4)_2\text{Fe}(\text{SO}_4)_2 \cdot 6\text{H}_2\text{O}$ (0.2 mmol L^{-1}) and Na_2SO_4 (0.05 mol L^{-1}) were dissolved in distilled water. $\text{Na}_2\text{MoO}_4 \cdot 2\text{H}_2\text{O}$ (0.003 mol L^{-1}) was then dissolved in a 0.5 mol L^{-1} H_2SO_4 (5 mL) solution. Finally, they were mixed and placed in a 500 mL volumetric flask and served as the electrodeposition solution. The ZnO nanoarrays were the working electrode. The electrodeposition process was carried out in a water bath heated to $70 \text{ }^\circ\text{C}$ and with stirring at 125 r min^{-1} . The electrodeposition time was approximately 80 min, and the current density was 0.5 mA cm^{-2} . For comparison, the remaining nanoarrays were synthesized via the same method. ZnO@Mo-MnO₂ NA were synthesized by omitting $(\text{NH}_4)_2\text{Fe}(\text{SO}_4)_2 \cdot 6\text{H}_2\text{O}$ from the composition, and the electrodeposition process took 55 min. ZnO@MnO₂ NA were synthesized by omitting $(\text{NH}_4)_2\text{Fe}(\text{SO}_4)_2 \cdot 6\text{H}_2\text{O}$ and $\text{Na}_2\text{MoO}_4 \cdot 2\text{H}_2\text{O}$ from the composition, and the electrodeposition process took 65 min. The carrier used for the electrodeposition process was the CC, and the electrodeposition process took 40 min. The synthesized active substance was identified as CC@Mo-Fe-MnO₂.

Preparation of piezoelectric films

PVDF-Trfe/CNT/BTO piezoelectric films were prepared with a simple casting method. 10 mg of CNTs, 20 mg of TNWDIS and 9 mL of DMF solvent were mixed in a beaker. After ultrasonication for 30 min to disperse the CNTs evenly, 1 g of PVDF-Trfe was added and stirred vigorously for 12 h. Then, 0.25 g of BTO was added and stirred vigorously again for 12 h. All stirring processes were carried out on a thermostatic table heated at $40 \text{ }^\circ\text{C}$. The resulting viscous solution was cast on a $70 \text{ }^\circ\text{C}$ constant temperature heated table with glass plates and spread evenly. After the solvent volatilized, PVDF-Trfe/CNT/BTO piezoelectric films were obtained. Finally, the PVDF-Trfe/CNT/BTO piezoelectric film was heated in an oil bath at $60 \text{ }^\circ\text{C}$ and poled under a 2000 V DC electric field for 2 h. The preparation method of PVDF-Trfe and PVDF-Trfe/CNTs films are the same as described above. The difference is was the CNTs, TNWDIS, BTO and BTO reagents were omitted from the components.

Preparation of H₃PO₄ gel electrolyte

PVA (4 g) was mixed with 40 mL of distilled water and heated and stirred until the PVA was completely dissolved and a homogeneous viscous solution was formed. Then, 4 mL of H_3PO_4 was added to the viscous solution and stirred until the solution cooled to room temperature.

Preparation of the SCSPC device

The SCSPC device was assembled with ZnO@Mo-Fe-MnO₂ NAs or CC@Mo-Fe-MnO₂ (1 cm×1 cm) as both the positive and negative electrodes. PVDF-Trfe/CNT/BTO piezoelectric films with ordered micropores were used as separators. A H₃PO₄ gel solution was used as the electrolyte in the assembled SCSPC device. The electrode was immersed in the H₃PO₄ gel electrolyte for 2 h under vacuum to completely contact the electrolyte with the surface of the electrode. The piezoelectric film was then sandwiched between the two electrodes and encapsulated with PI tape. The assembled SCSPC device was allowed to dry at 60 °C for 6 h. During the drying process, the SCSPC device was maintained under pressure.

Material characterizations

Phase analyses of the electrodes and piezoelectric films were performed with an XRD (D8ADVANCE-A25). The micromorphologies of the electrodes and piezoelectric films were detected with field emission SEM (Nova Nano SEM 450). The surface topographies and structures of the electrodes were analysed with TEM (FEIG2-20-TWIN). The elemental compositions and distributions of the electrodes were obtained with EDX spectrometry. The functional groups of the electrodes were determined with XPS (XPSINCA 250 X-max 50). The load of the electrode was weighed with a microelectronic balance (Mettler Toledo, XS205 Dual Range) of accuracy 0.1 mg. A digital multimeter (DMM 6500) by used to measure the open-circuit voltages of the piezoelectric films and the self-charging capabilities of the SCSPC devices. The piezoelectric film was poled with an ET2671A withstand voltage tester. An electrochemical workstation (CHI660e, Chenhua Shanghai) was used to determine the short-circuit currents of the piezoelectric films and the electrochemical capabilities of the electrodes. These included CV, GCD, and EIS. The experimental electrodeposition process was performed with an Advanced Electrochemical System (PARSTAT 2273). Long cycling lives of the assembled SCSPC devices were tested with an Arbin BT-2000 (#169483) system. The linear reciprocating motor was used to apply pressure.

Electrochemical measurements

The measurements for all as-prepared electrodes were performed with a three-electrode system (electrochemical workstation, CHI660e). The as-prepared electrode served as a working electrode, an SCE served as the reference electrode. A platinum metal sheet was used as the counter electrode. The measurements were performed in a 0.5 mol L⁻¹ Na₂SO₄ solution and at room temperature. The single electrode CV scan rates ranged from 2–100 mV s⁻¹, and the GCD measurement current densities were 1–100 A g⁻¹. The EIS measurements were performed over the frequency range 0.01–100000 Hz. The SCSPC device used a CV scan speed range of 10–200 mV s⁻¹ and GCD current densities of 15–100 μA cm⁻².

Supporting Information

Supporting Information is available from the Wiley Online Library or from the author. **Author Contributions**

Z.G.Y. conceived the idea of this study and designed the experiments. L.S. performed the sample synthesis. L.S. performed the material characterizations and electrochemical measurements. Z.G.Y., L.S., X.Y.P., S.J.Z., D.S.L. and Z.J. analyzed the data and discussed the results. Z.G.Y., Z.J. and L.S. co-wrote and revised the manuscript. Z.G.Y. supervised the project.

References

- [1] C. S. Wu, A. C. Wang, W. B. Ding, H. Y. Guo, Z. L. Wang, *Adv. Energy Mater.* **2019** , 9, 25.
- [2] K. Krishnamoorthy, P. Pazhamalai, S. Manoharan, N. U. L. Ali, S. J. Kim, *Carbon Energy* **2022** , 4, 833.
- [3] L. Manjakkal, C. G. Nunez, W. T. Dang, R. Dahiya, *Nano Energy* **2018** , 51, 604.
- [4] W. Yuan, C. G. Zhang, B. F. Zhang, X. L. Wei, O. U. Yang, Y. B. Liu, L. X. He, S. N. Cui, J. Wang, Z. L. Wang, *Adv. Mater. Technol.* **2022** , 7, 8.

- [5] J. Q. Zheng, Y. M. Wang, G. Liu, Z. H. Yu, S. Sun, Y. Fu, D. Chen, W. H. Cai, J. Q. Cui, G. S. Wang, H. M. Zhou, *J. Power Sources* **2022** , 528, 7.
- [6] A. Ramadoss, B. Saravanakumar, S. W. Lee, Y. S. Kim, S. J. Kim, Z. L. Wang, *ACS Nano* **2015** , 9, 4337.
- [7] H. X. He, Y. M. Fu, T. M. Zhao, X. C. Gao, L. L. Xing, Y. Zhang, X. Y. Xue, *Nano Energy* **2017** , 39, 590.
- [8] K. Krishnamoorthy, P. Pazhamalai, V. K. Mariappan, S. S. Nardekar, S. Sahoo, S. J. Kim, *Nat. Commun.* **2020** , 11, 11.
- [9] N. Chodankar, C. Padwal, H. D. Pham, K. Ostrikov, S. Jadhav, K. Mahale, P. Yarlagaadda, Y. S. Huh, Y. K. Han, D. Dubal, *Nano Energy* **2021** , 90, 12.
- [10] Y. Lu, Y. Jiang, Z. Lou, R. L. Shi, D. Chen, G. Z. Shen, *Prog. Nat. Sci.* **2020** , 30, 174.
- [11] S. Verma, S. Arya, V. Gupta, A. Khosla, *Chem. Eng. J.* **2021** , 424, 16.
- [12] H. Y. Wang, Q. Q. Zhou, B. W. Yao, H. Y. Ma, M. Zhang, C. Li, G. Q. Shi, *Adv. Mater. Interfaces* **2018** , 5, 7.
- [13] D. Zhou, F. Y. Wang, X. D. Zhao, J. Q. Yang, H. R. Lu, L. Y. Lin, L. Z. Fan, *ACS Appl. Mater. Interfaces* **2020** , 12, 44883.
- [14] I. Rabani, Y. J. Park, J. W. Lee, M. S. Tahir, A. Kumar, Y. S. Seo, *J. Mater. Chem. A* **2022** , 10, 15580.
- [15] B. Padha, S. Verma, S. Arya, *Adv. Mater. Technol.* **2022** , 7, 13.
- [16] S. B. Liu, A. L. Li, C. G. Yang, F. P. Ouyang, J. F. Zhou, X. L. Liu, *Appl. Surf. Sci.* **2022** , 571, 11.
- [17] X. Y. Zhang, Q. G. Fu, H. M. Huang, L. Wei, X. Guo, *Small* **2019** , 15, 13.
- [18] Q. Hu, X. L. Jiang, M. He, Q. J. Zheng, K. H. Lam, D. M. Lin, *Electrochim. Acta* **2020** , 338, 10.
- [19] K. Q. Wu, Z. G. Ye, Y. Ding, Z. X. Zhu, X. Y. Peng, D. S. Li, G. Ma, *J. Power Sources* **2020** , 477, 10.
- [20] Y. Jin, H. Y. Chen, M. H. Chen, N. Liu, Q. W. Li, *ACS Appl. Mater. Interfaces* **2013** , 5, 3408.
- [21] Y. P. Tian, C. H. Yang, W. X. Que, X. B. Liu, X. T. Yin, L. B. Kong, *J. Power Sources* **2017** , 359, 332.
- [22] M. H. Zhao, Z. L. Wang, S. X. Mao, *Nano Lett.* **2004** , 4, 587.
- [23] Y. Qin, X. D. Wang, Z. L. Wang, *Nature* **2008** , 451, 809.
- [24] Z. L. Wang, J. H. Song, *Science* **2006** , 312, 242.
- [25] V. Cauda, S. Stassi, A. Lamberti, M. Morello, C. F. Pirri, G. Canavese, *Nano Energy* **2015** , 18, 212.
- [26] X. Zheng, K. Zhang, Y. H. Sun, S. J. Jin, Y. Li, H. Yu, H. Y. Qin, Y. Y. Ding, *Journal of Alloys and Compounds* **2021** , 851, 5.
- [27] C. Y. Zhao, X. D. Sun, W. S. Li, M. W. Shi, K. L. Ren, X. M. Lu, *ACS Appl. Energ. Mater.* **2021** , 4, 8070.
- [28] Y. Mallaiah, V. R. Jeedi, R. Swarnalatha, A. Raju, S. N. Reddy, A. S. Chary, *J. Phys. Chem. Solids* **2021** , 155, 8.
- [29] A. V. Solnyshkin, I. L. Kislova, I. M. Morsakov, A. N. Belov, V. I. Shevyakov, D. A. Kiselev, V. V. Shvartsman, *Journal of Advanced Dielectrics* **2017** , 07, 1720003.
- [30] B. Singh, B. Padha, S. Verma, S. Satapathi, V. Gupta, S. Arya, *J. Energy Storage* **2022** , 47, 24.

- [31] S. J. Zhuang, X. Y. Peng, F. Pei, L. Sun, Z. G. Ye, J. T. Huang, D. S. Li, Z. Jin, *Sci. China-Mater.* **2023** , DOI: 10.1007/s40843-022-2353-x9.
- [32] X. Li, Z. Zhu, G. Ma, Y. Ding, J. Wang, Z. Ye, X. Peng, D. Li, *Journal of Electronic Materials* **2022** , 51, 2982.
- [33] K. Q. Wu, X. Q. Li, Z. X. Zhu, G. Ma, Y. Ding, J. L. Wang, Z. G. Ye, X. Y. Peng, D. S. Li, Z. Jin, *J. Mater. Sci.-Mater. Electron.* **2022** , 33, 13326.
- [34] Y. Niu, H. Su, X. Li, J. Li, Y. Qi, *Journal of Alloys and Compounds* **2022** , 898, 162863.
- [35] D. Zhou, F. Y. Wang, J. Q. Yang, L. Z. Fan, *Chem. Eng. J.* **2021** , 406, 9.
- [36] W. J. Lee, K. H. Kim, Y. J. Choi, Z. X. Wan, S. H. Kwon, *Energy Technol.* **2023** , DOI: 10.1002/ente.20220112011.
- [37] Q. Ma, M. Yang, X. H. Xia, H. Chen, L. Yang, H. B. Liu, *Electrochim. Acta* **2018** , 291, 9.
- [38] T. Zhai, S. L. Xie, M. H. Yu, P. P. Fang, C. L. Liang, X. H. Lu, Y. X. Tong, *Nano Energy* **2014** , 8, 255.
- [39] M. Lu, Y. Cao, Y. Xue, W. Qiu, *ACS omega* **2021** , 6, 27994.
- [40] M. Li, A. Addad, M. Dolci, P. Roussel, M. Naushad, S. Szunerits, R. Boukherroub, *Chem. Eng. J.* **2020** , 396, 9.
- [41] L. M. Qin, G. Y. Yang, D. Li, K. T. Ou, H. Y. Zheng, Q. Fu, Y. Y. Sun, *Chem. Eng. J.* **2022** , 430, 10.
- [42] X. Ji, H. W. Luo, W. J. Dong, L. X. Yang, J. J. Guo, S. Cheng, *Electrochim. Acta* **2023** , 449, 8.
- [43] N. Jabeen, A. Hussain, Q. Y. Xia, S. Sun, J. W. Zhu, H. Xia, *Adv. Mater.* **2017** , 29, 9.
- [44] Y. Zhao, S. C. Wang, M. Yuan, Y. Chen, Y. P. Huang, J. B. A. Lian, S. L. Yang, H. M. Li, L. M. Wu, *Chem. Eng. J.* **2021** , 417, 9.
- [45] S. Hussain, I. Rabani, D. Vikraman, A. Feroze, M. Ali, Y. S. Seo, W. S. Song, K. S. An, H. S. Kim, S. H. Chun, J. Jung, *Chem. Eng. J.* **2021** , 421, 15.
- [46] Q. T. Nguyen, U. T. Nakate, J. Chen, D. T. Tran, S. Park, *Composites Part B: Engineering* **2023** , 110528.
- [47] Y. Duan, Z. Y. Yu, S. J. Hu, X. S. Zheng, C. T. Zhang, H. H. Ding, B. C. Hu, Q. Q. Fu, Z. L. Yu, X. Zheng, J. F. Zhu, M. R. Gao, S. H. Yu, *Angew. Chem.-Int. Edit.* **2019** , 58, 15772.
- [48] R. Zhang, J. W. Yan, L. Wang, W. Z. Shen, J. L. Zhang, M. Zhong, S. W. Guo, *J. Power Sources* **2021** , 513, 9.
- [49] M. N. Sakib, S. Ahmed, S. Rahat, S. B. Shuchi, *J. Energy Storage* **2021** , 44, 31.
- [50] Y. F. Huang, T. Gu, G. C. Rui, P. R. Shi, W. B. Fu, L. Chen, X. T. Liu, J. P. Zeng, B. H. Kang, Z. C. Yan, F. J. Stadler, L. Zhu, F. Y. Kang, Y. B. He, *Energy Environ. Sci.* **2021** , 14, 6021.
- [51] Y. H. Ye, Y. F. Zhang, Y. Chen, X. S. Han, F. Jiang, *Adv. Funct. Mater.* **2020** , 30, 12.
- [52] S. Manoharan, P. Pazhamalai, V. K. Mariappan, K. Murugesan, S. Subramanian, K. Krishnamoorthy, S. J. Kim, *Nano Energy* **2021** , 83, 11.
- [53] K. Krishnamoorthy, S. Manoharan, V. K. Mariappan, P. Pazhamalai, S. J. Kim, *J. Mater. Chem. A* **2022** , 10, 7818.
- [54] P. Pazhamalai, K. Krishnamoorthy, V. K. Mariappan, S. Sahoo, S. Manoharan, S. J. Kim, *Adv. Mater. Interfaces* **2018** , 5, 9.

- [55] K. Shrestha, S. Sharma, G. B. Pradhan, T. Bhatta, S. S. Rana, S. H. Y. Lee, S. Seonu, Y. Shin, J. Y. Park, *Nano Energy* **2022** , 102, 12.
- [56] P. Pazhamalai, K. Krishnamoorthy, S. Manoharan, V. K. Mariappan, S. J. Kim, *Sustain. Mater. Technol.* **2022** , 33, 11.
- [57] H. H. Singh, S. Singh, N. Khare, *Polym. Adv. Technol.* **2018** , 29, 143.
- [58] S. Mondal, S. Thakur, S. Maiti, S. Bhattacharjee, K. K. Chattopadhyay, *ACS Appl. Mater. Interfaces* **2023** , DOI: 10.1021/acsami.2c1753816.
- [59] S. Bairagi, S. W. Ali, *Soft Matter* **2020** , 16, 4876.
- [60] K. Y. Fang, F. Fang, S. W. Wang, W. Yang, W. Sun, J. F. Li, *J. Phys. D-Appl. Phys.* **2018** , 51, 8.
- [61] Y. M. You, W. Q. Liao, D. W. Zhao, H. Y. Ye, Y. Zhang, Q. H. Zhou, X. H. Niu, J. L. Wang, P. F. Li, D. W. Fu, Z. M. Wang, S. Gao, K. L. Yang, J. M. Liu, J. Y. Li, Y. F. Yan, R. G. Xiong, *Science* **2017** , 357, 306.
- [62] Z. X. Wang, W. Q. Liao, *Science* **2022** , 375, 1353.
- [63] D. Zhou, N. Wang, T. T. Yang, L. Wang, X. Cao, Z. L. Wang, *Mater. Horizons* **2020** , 7, 2158.
- [64] X. Y. Gao, Y. Z. Zhang, Y. F. Zhao, S. K. Yin, J. Z. Gui, C. L. Sun, S. S. Guo, *Nano Energy* **2022** , 91, 14.

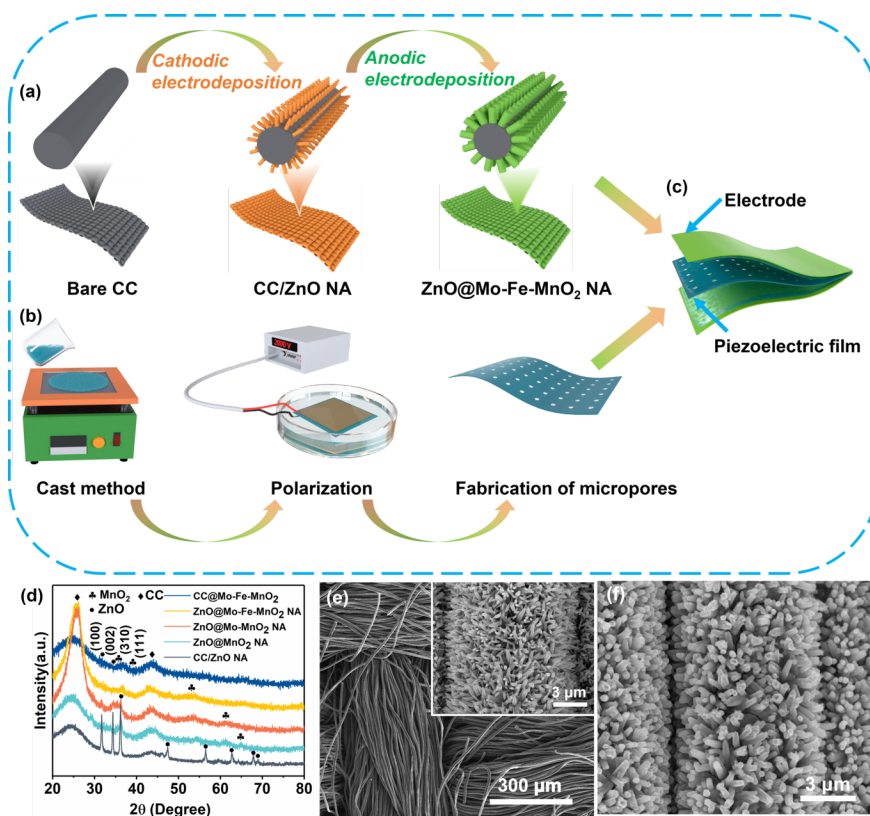


Figure 1. Schematic diagram of the preparation procedures of (a) the ZnO@Mo-Fe-MnO₂ NA electrode and (b) the PVDF-Trfe/CNTs/BTO piezoelectric film, and (c) the SCSPC device. (d) XRD diffraction

patterns of the prepared electrodes and current collectors. SEM images of (e) CC and CC/ZnO NAs and (f) the ZnO@Mo-Fe-MnO₂ NAs.

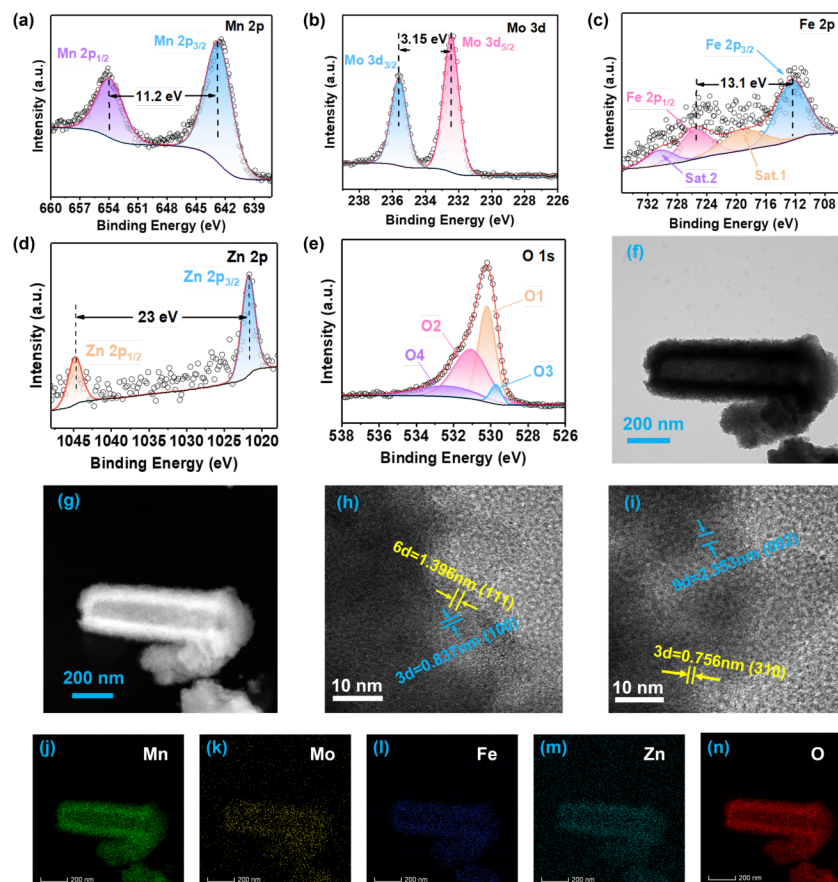


Figure 2. (a) Mn 2p, (b) Mo 3d, (c) Fe 2p, (d) Zn 2p and (e) O 1s XPS data of the ZnO@Mo-Fe-MnO₂ NAs. (f) TEM, (g) STEM, (h, i) HRTEM images, (j-n) corresponding EDX elemental mappings at Mn, Mo, Fe, Zn, O regions of the ZnO@Mo-Fe-MnO₂ NAs, respectively.

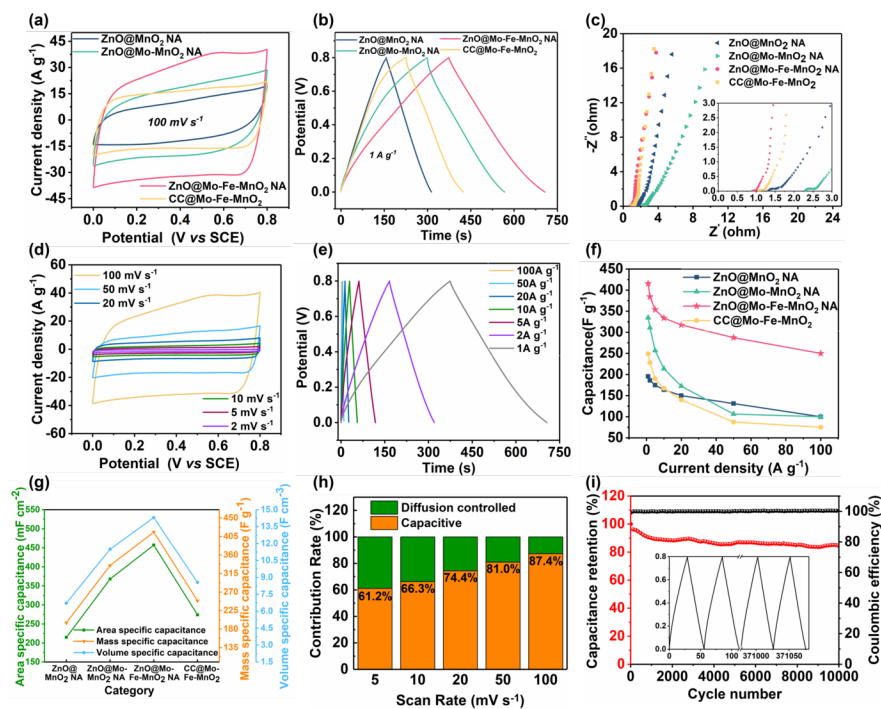


Figure 3. Electrochemical performances of the as-prepared electrodes. (a) CV curves of all as-prepared electrodes at a scan rate of 100 mV s^{-1} . (b) GCD curves of all as-prepared electrodes at a current density of 1 A g^{-1} . (c) Nyquist plots measured in the frequency range 10^5 - 0.01 Hz for all as-prepared electrodes. (d) CV curves generated at the scan rates ranged in 2 - 100 mV s^{-1} . (e) GCD curves with different current densities of the ZnO@Mo-Fe-MnO₂ NA electrode. (f) Specific capacitance comparison of the as-prepared electrodes over a current density range of 1 - 100 A g^{-1} . (g) The mass, area and volume capacitances of the as-prepared electrodes at a current density of 1 A g^{-1} . (h) Capacitance contributions, (i) cycling performance and Coulombic efficiency of the ZnO@Mo-Fe-MnO₂ NA electrode.

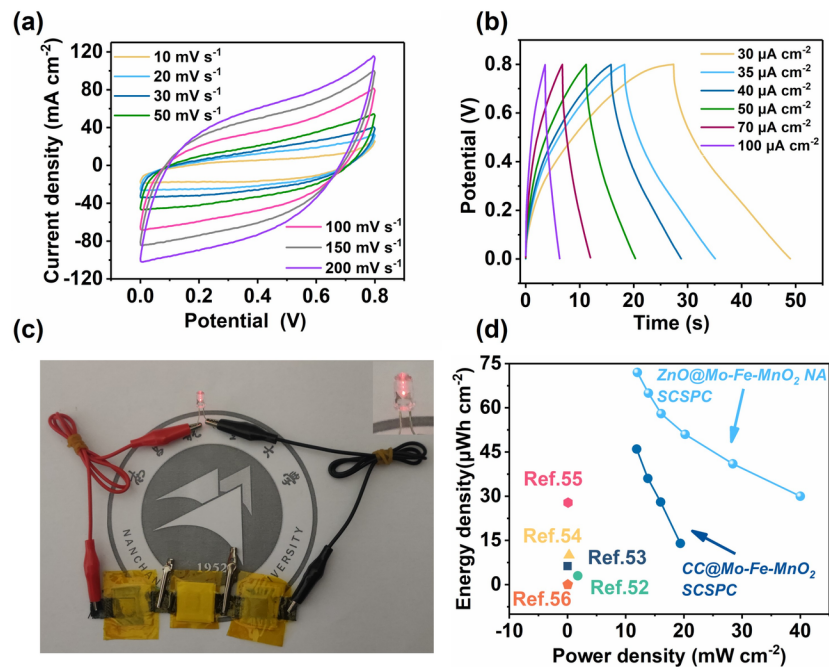


Figure 4. (a) CV curves and (b) GCD curves of the ZnO@Mo-Fe-MnO₂ NA based SCSPC. (c) Three series-connected ZnO@Mo-Fe-MnO₂ NA based SCSPC devices lit up a red LED. (d) Ragone plots of the SCSPC device in this study compared with previous works.

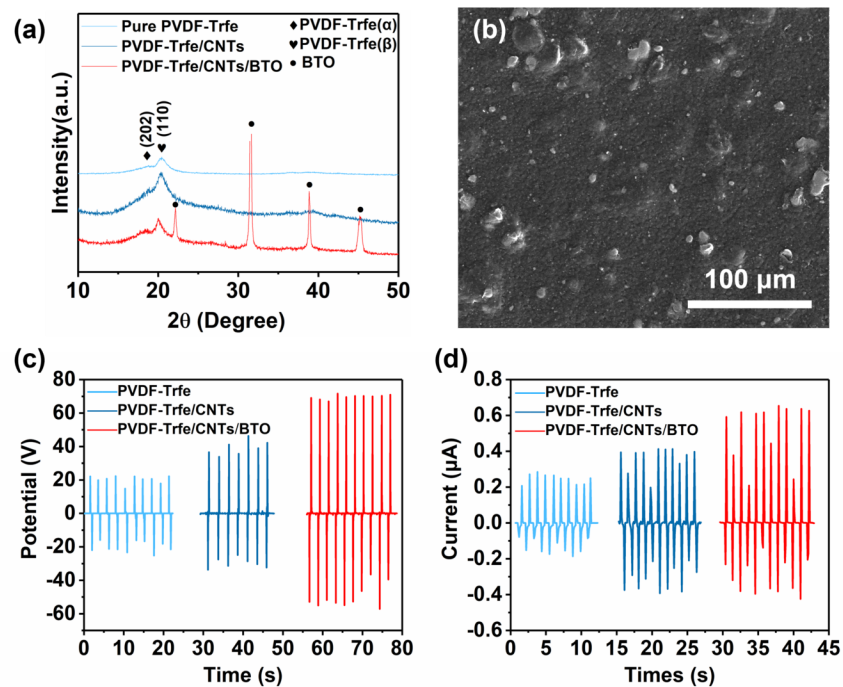


Figure 5. (a) XRD patterns of the PVDF-Trfe, PVDF-Trfe/CNT and PVDF-Trfe/CNT/BTO piezoelectric films. (b) Surface SEM image of the PVDF-Trfe/CNTs/BTO piezoelectric film. (c) Open-circuit voltage and (d) current vs. time for the three samples.

and (d) short-circuit current of the PVDF-Trfe, PVDF-Trfe/CNT and PVDF-Trfe/CNT/BTO piezoelectric films, respectively.

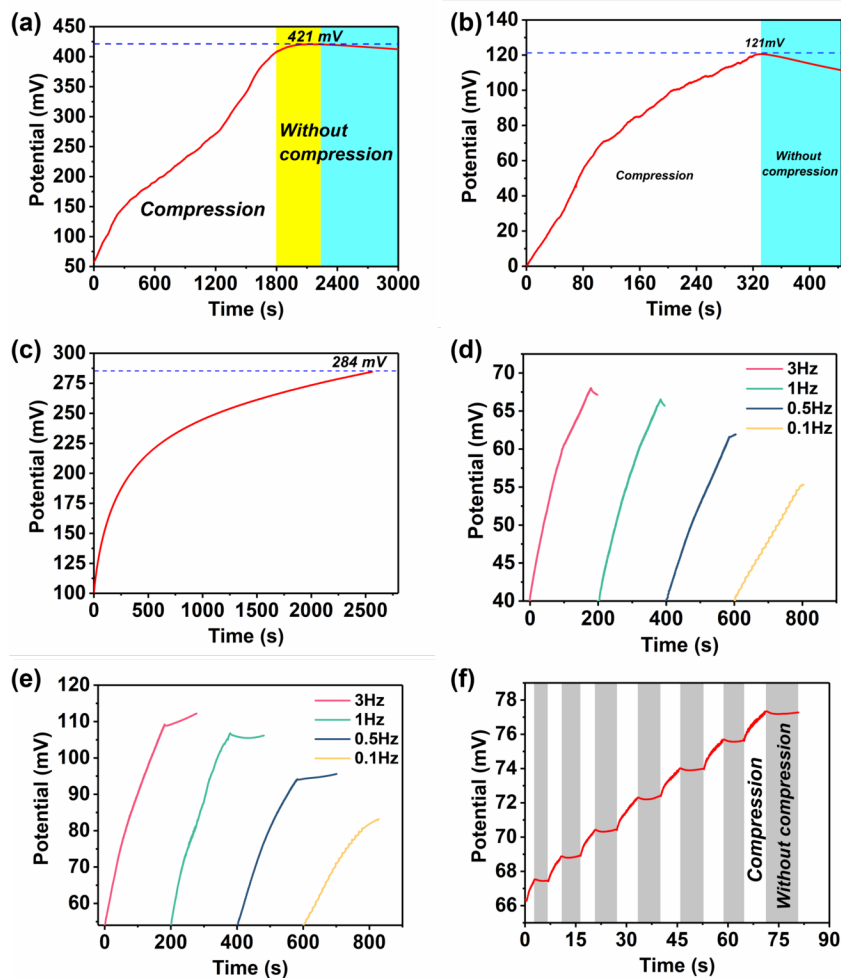


Figure 6. (a) Self-charging performance of the ZnO@Mo-Fe-MnO₂ NA based SCSPC devices. (b) Self-charging performance of the CC@Mo-Fe-MnO₂ based SCSPC devices. (c) Self-charging curves resulting from residual stress, (d) self-charging performance with a 1 N force, (e) self-charging performance with a 10 N force, and (f) stepwise self-charging curve of a ZnO@Mo-Fe-MnO₂ NA based SCSPC device.

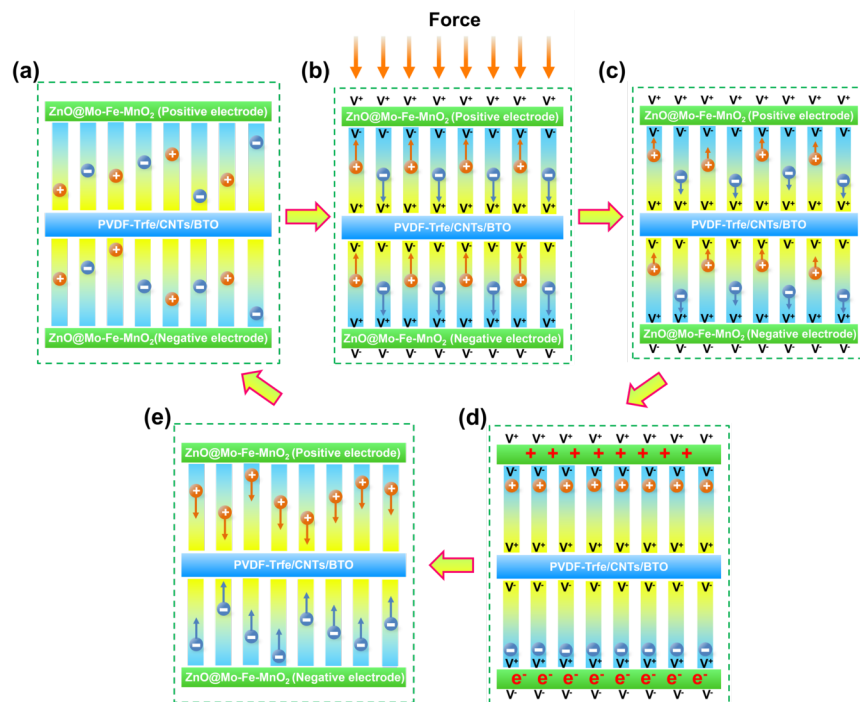


Figure 7. Self-charging mechanism of the ZnO@Mo-Fe-MnO₂ NA based SCSPC. **(a)** The original state of the device without external forces. **(b)** The potential difference created by the external force drove the mobility of the electrolyte ions. **(c)** The potential difference resulting from the residual stress caused the electrolyte ions to migrate again. **(d)** A new electrochemical equilibrium was reached. **(e)** The positive and negative potentials disappeared, and the counter migration of electrolyte ions occurred and returned to the original states.